Mechanical Systems and Signal Processing 162 (2022) 108047

Contents lists available at ScienceDirect

Mechanical Systems and Signal Processing

journal homepage: www.elsevier.com/locate/ymssp

Topological cavities in phononic plates for robust energy harvesting

Zhihui Wen [a], Yabin Jin [a,*], Penglin Gao [b,*], Xiaoying Zhuang [c,d], Timon Rabczuk [e], Bahram Djafari-Rouhani [f]

[a] *School of Aerospace Engineering and Applied Mechanics, Tongji University, 200092 Shanghai, China*
[b] *Department of Physics, Universidad Carlos III de Madrid, ES-28916 Leganes, Madrid, Spain*
[c] *Department of Geotechnical Engineering, College of Civil Engineering, Tongji University, 200092 Shanghai, China*
[d] *Institute of Photonics, Department of Mathematics and Physics, Leibniz University Hannover, Germany*
[e] *Institute of Structural Mechanics, Bauhaus-Universität Weimar, Weimar D-99423, Germany*
[f] *Institut d'Electronique, de Microélectonique et de Nanotechnologie, UMR CNRS 8520, Département de Physique, Université de Lille, 59650 Villeneuve d'Ascq, France*

A R T I C L E I N F O

Communicated by Ioannis Kougioumtzoglou

Keywords:
Topological cavity
Phononic thin plate
Energy harvesting
Robustness
Piezoelectricity

A B S T R A C T

Piezoelectric energy harvesting has attracted tremendous interest for designing sustainable self-powered devices/systems targeted to special environment such as wireless or wearable applications. The traditional cavity (e.g., phononic cavity mode) excitation is highly applicable in terms of sufficient power generation, nevertheless, has to endure the drawback of extremely poor robustness intrinsic to the trivial cavity modes. We propose to use phononic thin plate systems for robust energy harvesting application relying on zero-dimensional cavities confined by the Kekulé distorted topological vortices. The harvesting power induced by topological cavities is about 30 times that of the bare plate. Further studies on the effects of deliberately introduced defects on the output power show that the proposed energy harvesting system is highly robust against symmetry-preserving defects, and is less influenced even for symmetry-breaking defects at moderate perturbation level. Beyond the reported energy harvesting application, we foresee that our work may open avenues for robust operations in the realm of wireless sensing and structural health monitoring.

1. Introduction

The phononic crystals and mechanical metamaterials are artificial structures having both periodic and aperiodic configurations [1–4], which can prevent acoustic or elastic wave propagation by creating bandgaps. This property plays a key role in the manipulation of acoustic or elastic waves, such as confinement effect [5,6] and waveguiding [7,8]. In phononic thin plates, the flexural wave modes in the bandgap can be captured with defects in phononic crystals and metamaterials [9–11]. The localized mode caused by the removal of scatters/resonators is termed as cavity mode, which has been widely used for energy harvesting [9,12–17]. The energy harvesting usually relies on coupling the out-of-plane bending strain and the piezoelectric effect of piezoelectric patch fixed at the defect position [12,18]. Energy harvesting is achievable for both sonic [13,15] and mechanical vibrations [12]. Acoustic/elastic energy harvesting has

* Corresponding authors.
E-mail addresses: 083623jinyabin@tongji.edu.cn (Y. Jin), gplhit@gmail.com (P. Gao).

https://doi.org/10.1016/j.ymssp.2021.108047
Received 13 November 2020; Received in revised form 25 March 2021; Accepted 11 May 2021
Available online 29 May 2021

Nomenclature

$\boldsymbol{R}$	Unperturbed distance of adjacent resonators
a_0	Primitive lattice period
$\boldsymbol{k}_0$	Kekulé wave vector
ϕ	Kekulé phase
A_i	Distortion amplitude
$\boldsymbol{\xi}_i$	Vortex radius
n	Vorticity
a	Lattice constant
E	Young's modulus of thin plate
ρ	Density of thin plate
ν	Poisson's ratio of thin plate
E_n	Young's modulus of neck
ρ_n	Density of neck
ν_n	Poisson's ratio of neck
E_h	Young's modulus of resonator head
ρ_h	Density of resonator head
ν_h	Poisson's ratio of resonator head
h	Plate thickness
h_n	Height of neck
d_n	Diameter of neck
h_h	Height of resonator head
d_h	Diameter of resonator head
D	Plate stiffness
ω	Angular frequency
$\mathrm{m_R}$	Mass of resonator head
k_n	Effective stiffness of resonator neck
K	Bloch wave vector
$\boldsymbol{G}$	Reciprocal lattice vector
$\boldsymbol{g}_i$	Basis vector of reciprocal space
$\boldsymbol{a}_i$	Basis vector of primitive space
δ_{ij}	Kronecker symbol
S	Area of unit cell
w	Out-of-plane displacement of thin plate
w_1	Out-of-plane displacement of resonator
Ω	Normalized frequency
γ_α	Normalized mass
t_i	Stiffness coefficient
f	Excitation frequency
G_0	Green function
Λ	Scattering coefficients of resonator
Rd	Radius of distortion structure
L	Side length of PZT
S_{ij}	Strain of PZT
V	Electrical voltage
E_z	The z-component of electric field
ε_0	Vacuum permittivity
e_{3i}	Piezoelectric ceramic constant
t	Thickness of PZT layer
R_0	Resistance of AC electrical circuit
I	Current amplitude
P	Average harvesting power
AC	Alternating current

been reported by employing point defect of resonant cavity [13,19], piezoelectric beam [14,20–22], planar acoustic metamaterial [15] and so forth. Besides, deep sub-wavelength elastic wave [9,23] and wide working bandgap by double defect mode [24] have been investigated for energy harvesting. The factors that affect energy harvesting are important. Therefore, the supercell size and defect location of defect mode [25] have been studied in depth for energy localization and harvesting. Recently, graded elastic metasurface

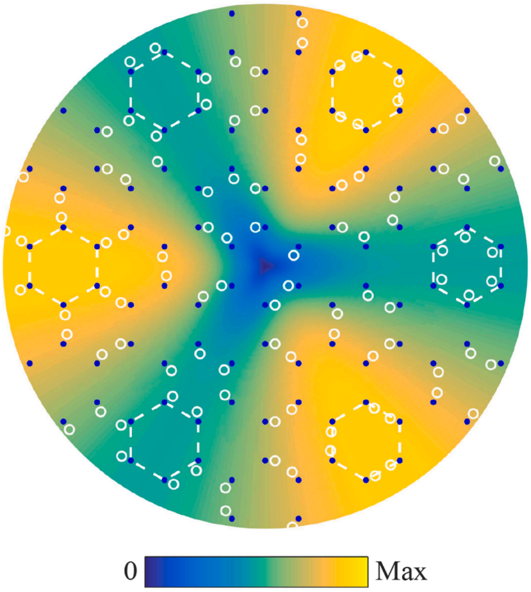

Fig. 1. Mechanical analogue of Jackiw-Rossi vortex whose Kekulé phase has a winding number $n = 1$ [42,47]. Resonators are arranged in honeycomb lattice to introduce intervalley coupling. The blue solid dots and white hollow circles denote, respectively, the lattice sites (resonators) in the primitive and disturbed lattices. The background color map illustrates the bandgap width distribution induced by the position-dependent Kekulé modulation.

[16] and octagonal phononic crystals [12] were employed to further enhance the energy harvesting of elastic waves in thin plates.

In the past decades, the utilization of cavity modes for energy harvesting was the mainstream and allowed tremendous achievements in this field. However, the robustness of the cavity mode against unintentionally introduced perturbations, such as the variation of geometric parameters and material properties introduced during the additive manufacturing process [26], is relatively weak. On the other hand, cavity mode is destined to be casual and unpredictable in the sense that whose frequency is quite sensitive to relatively small parameter variations. The rise of topological phases [27–30] for classical waves opens new routes to reexamine the aforementioned challenging problems. Along with the development of topological phases in condensed matter physics, we have recently witnessed a booming frontier for classical systems, such as acoustic topological insulator [31–34], topological bound states of elastic waves [35], topological pumping [36] and higher-order topological insulators [37]. On the other hand, the corner modes depended on the higher-order topological insulators have been widely concerned in 2D and 3D systems recently [38–40]. The responses of the metamaterials are firmly fixed at the corners of them. The aforementioned topological phases provided a rich and diverse choice for acoustic, vibrational and optical implementations.

Apart from the uniform higher-order topological insulators, as initially suggested by Jackiw and Rossi [41], aperiodic topological vortex hosts lower-dimensional bound states as well, which has been experimentally verified very recently in classical systems for sound, vibration and light [42–44]. The key point lies in the complex intervalley coupling that is readily accessible thanks to the Kekulé modulation mechanism which, in a nutshell, relies on hybridizing valley modes via the band-folding mechanism [45,46]. The latest topological bound states of acoustics [42,47], mechanics [43] and optics [44,48] are also based on the binding mechanism, and lead to the exact bound confinement of acoustic / elastic / optical waves at the vortex core. The bound states can be excited exactly at Dirac frequency when a point source is placed near the vortex center. The abundant designable parameters, the strong robustness and the wide range of operating conditions of the binding mechanism open a new way for energy harvesting applications. Along the frontier of topological physics, Chaplain et al. [49] recently proposed a 1D graded SSH model and utilized its interface state for energy harvesting. Here, we utilize the Jackiw-Rossi binding mechanism to trap and harvest elastic energy from 2D plate, which is fundamentally different from the 1D implementation.

We deepen the reach of topological bound states for energy harvesting via the Kekulé modulation. In Sec. 2, we design the topological vortex mechanical thin plates with the exact zero bandgap at the vortex core based on honeycomb lattice. And then in Sec. 3, we develop the numerical tools for analyzing, including the dispersion theory, multiple scattering theory and piezoelectric effect theory. Sec. 4 is committed to the realization of the topological peak of the piezoelectric output power, which is our primary pursuit. In Sec. 5, we systematically study the robustness of power peaks of mechanical thin plates against the minor disturbances including both the symmetry-preserving and symmetry-breaking defects. And last Sec. 6 gives the conclusion.

2. Modeling of topological vortex in phononic thin plates

As illustrated in Fig. 1, we start with a honeycomb lattice consisting of spring-mass resonators (blue dots) that are attached to a thin plate to build a mechanical plate system. Thanks to the spatial inversion symmetry, such lattices naturally sustain Dirac dispersion at

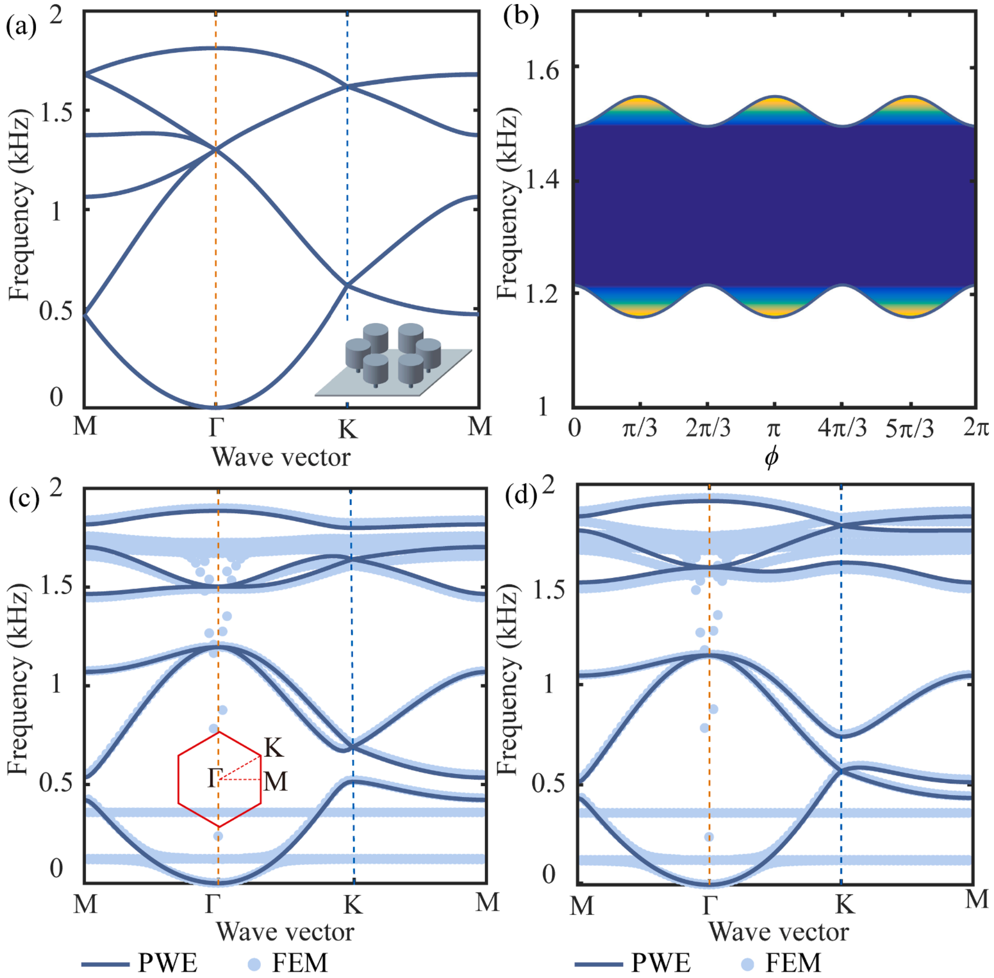

Fig. 2. (a) Band diagrams of flexural waves propagating in the unperturbed honeycomb lattice (see the inset for its supercell). (b) Bandgap variation of a uniform Kekulé lattice when its phase is increased from 0 to 2π at constant distortion amplitude A_0=0.12a_0. Band diagrams calculated with the self-developed PWE algorithm and the finite element simulations for two typical scenarios: (c) $\phi = 0$; (d) $\phi = \pi$. The Brillouin zone and high symmetry points are illustrated in the inset of panel (c).

the Brillouin corners, i.e., K and K' points, which facilitates the exploration of graphene-like physics for flexural vibrations [50]. The two valleys degree of freedom are mutually independent and cannot be coupled together in the pristine honeycomb lattices. Fortunately, the Kekulé distortion which relies on expanding supercells opens an avenue to acquire complex intervalley coupling that is at the core of topological vortex realization. The physics is because the expanded supercell folds the two valleys to appear simultaneously at the Brillouin zone center hence giving rise to valley modes hybridization [45]. As proposed by Jackiw and Rossi [41] topological bound states are expected to appear at a vortex center if the complex intervalley coupling is modulated to be position-dependent together with the phase winding process. This speculation has recently been experimentally demonstrated in both sonic [42] and mechanical systems [43] by employing generalized Kekulé modulation to introduce the required phase controlled intervalley coupling. Here we follow the implementation of Chen et al. [43] to explore the appealing applications of such topological bound state for robust energy harvesting. We now use expanded supercells whose six resonators (blue solid dots) are displaced to form Kekulé texture of different phases (white hollow circles), as highlighted by the hexagons around the perimeter in Fig. 1. Around the center the Kekulé phase winding eventually leads to a topological vortex composing aperiodic lattice sites

$$\boldsymbol{R}(\boldsymbol{r}_{i\alpha}) = \boldsymbol{r}_{i\alpha} - \Delta(\boldsymbol{r}_{i\alpha})\{sin[\boldsymbol{k}_0\cdot\boldsymbol{r}_{i\alpha}+\phi(\boldsymbol{r}_{i\alpha})],\ \varphi(\alpha)cos[\boldsymbol{k}_0\cdot\boldsymbol{r}_{i\alpha}+\phi(\boldsymbol{r}_{i\alpha})]\},\tag{1}$$

where $\boldsymbol{r}_{i\alpha} = [x_{i\alpha}, y_{i\alpha}]$ is the position vector of the primitive lattice sites with subscripts i and α denoting the unit cell and sublattice indices, respectively. We emphasize that the y-component distortion is differentiated with $\varphi(\alpha) = \pm 1$ for the two sublattices. In Eq. (1), we have introduced two position-dependent terms to ensure smooth lattice variation around the vortex center. One is the position distortion $\Delta(\boldsymbol{r}_{i\alpha}) = A_0 tanh(|\boldsymbol{r}_{i\alpha}|/\xi_0)$ which controls the gap opening process along the radial direction by tuning both its amplitude A_0 and vortex radius ξ_0. Another ingredient is the Kekulé phase $\phi(\boldsymbol{r}_{i\alpha}) = n\theta$ whose angular winding embodies an adiabatic pumping process responsible for the emergence of topological bound states [47]. In this study, the involved parameters are specified as: the distance between two nearest resonators $R = 16$ mm, primitive lattice period $a_0 = \sqrt{3}R$, winding number $n = 1$, Kekulé wave vector $\boldsymbol{k}_0 = [4\pi/3a_0, 0]$, distortion amplitude $A_0 = 0.12a_0$ and vortex radius $\xi_0 = 0.1a_0$.

For clarity, we have a closer look at the expanded supercell with constant Δ and ϕ, serving as building blocks of the Kekulé distorted vortex, to reveal the gap-opening process. In Fig. 1, the background color illustrates the gap width distribution (subwavelength Bragg band gaps [51,52]) along with the modulation of $\Delta(\boldsymbol{r}_{i\alpha})$ and $\phi(\boldsymbol{r}_{i\alpha})$. What clearly stands out is the gapless core ($\Delta = 0$) from which the gap width increases with radial coordinate until reaching a saturation value, while it shows periodic features during the angular variation. Such bandgap pattern will allow the construction of a robust bound state at the vortex core [42,43], which is very useful for designing topologically mechanical devices for sensing and energy harvesting.

3. Methodology

To derive the theory of the mechanical metamaterial for energy harvesting, we briefly introduce the classical Kirchhoff-Love thin plate theory of flexural waves and describe the methodology. We emphasize that the numerical tools developed here are not suitable for thick plate problems that have to employ the Mindlin-Reissner theory [53,54]. The resonators in honeycomb lattice are connected to the thin aluminum plate through necks [see the inset in Fig. 2(a)]. Throughout this work, if not specified, the thickness of the aluminum plate h is 1 mm, whose elastic parameters are Young's modulus $E = 73$ GPa, Poisson's ratio $\nu = 0.352$ and density $\rho = 2730\ \mathrm{kg\cdot m^{-3}}$. The resonator's cylinder neck is made of resin with height $h_n = 5$ mm and diameter $d_n = 2$ mm, whose elastic parameters are Young's modulus $E_n = 2.65$ GPa, Poisson's ratio $\nu_n = 0.41$ and density $\rho_n = 1095.24\ \mathrm{kg\cdot m^{-3}}$. The resonator head is made of lead (Young's modulus $E_h = 16$ GPa, Poisson's ratio $\nu_h = 0.42$ and density $\rho_h = 11370\ \mathrm{kg\cdot m^{-3}}$) with height $h_h = 12.66$ mm and diameter $d_h = 8$ mm. The material properties mentioned above are based on standard commercial materials that are isotropic and with extremely small to negligible viscoelastic damping. The designed effects shown in this work are mainly related to the geometrical parameters rather than to the material properties. Therefore, other solid materials can also be applicable.

3.1. Dispersions

Plane wave expansion method (PWE) has becoming a widely used tool for band diagram computation [55,56]. If properly extended, such method is useful for analyzing even evanescent Bloch waves [53,57,58]. With this method, here we first evaluate the dispersion curves of uniform Kekulé lattices. The unperturbed lattice sites are $\boldsymbol{R}_{i\alpha} = \boldsymbol{R}_i + \boldsymbol{R}_\alpha$, where i runs for all the lattice vectors and α runs for all the six resonators within the supercell. It should be noted that the honeycomb lattice represents a supercell with respect to the primitive cell with two resonators as mentioned in Sec. 2. The transition folds the dispersion curves inside the bigger Brillouin zone of the primitive cell into the smaller Brillouin zone of the supercell [59]. In the PWE theory, we consider the honeycomb lattice with a lattice constant $a = 3R$ to create a double Dirac cone at the Γ point of the Brillouin zone for further construction of topological bound states. The equation of motion for flexural waves in the mechanical metamaterial thin plate can be written as [60,61]

$$(D\nabla^4 - \omega^2\rho h)w(\boldsymbol{r}) = \sum_{R_i,\alpha}\omega^2 m_R w_1(\boldsymbol{R}_{i\alpha})\delta(\boldsymbol{r}-\boldsymbol{R}_{i\alpha}), \tag{2}$$

where D is the plate stiffness, ∇^4 is the biharmonic operator, $w(\boldsymbol{r})$ is the out-of-plane displacement and ω is the angular frequency. The summation runs over all resonator sites within the expanded supercell. Resonator head is boiled down to lumped masses $m_R = \pi d_h^2 h_h/4$, and the resonator neck is simplified as a linear elastic spring with a stiffness $k_n = \pi E_n d_n^2/4h_n$ [51]. According to Newton's second law and the coordination equation of the system, the governing equation of each resonator is

$$\omega^2 m_R w_1(\boldsymbol{R}_{i\alpha}) = -k_n(w(\boldsymbol{R}_{i\alpha}) - w_1(\boldsymbol{R}_{i\alpha})). \tag{3}$$

By the derivation of Floquet-Bloch waves in periodic systems (see Appendix A), the above equations are rewritten in matrix form

$$\left(\begin{bmatrix}\boldsymbol{P}_{11} & \boldsymbol{P}_{12}\\ \boldsymbol{P}_{21} & \boldsymbol{P}_{22}\end{bmatrix} - \Omega^2\begin{bmatrix}\boldsymbol{Q}_{11} & \boldsymbol{0}\\ \boldsymbol{0} & \boldsymbol{Q}_{22}\end{bmatrix}\right)\times\begin{pmatrix} w(\boldsymbol{G})\\ w_1(\boldsymbol{0}_\alpha)\end{pmatrix} = 0, \tag{4}$$

with notations

$$\boldsymbol{P}_{11}(ij) = \left((k_x+G_{xi})^2 + (k_y+G_{yi})^2\right)^2 a^4\delta_{ij} + \sum_\alpha \gamma_\alpha\Omega_\alpha^2 e^{-j(\boldsymbol{G}_i-\boldsymbol{G}_j)\cdot\boldsymbol{R}_\alpha}\ ,\ \boldsymbol{P}_{12}(i\alpha) = -\gamma_\alpha\Omega_\alpha^2 e^{-j\boldsymbol{G}_i\cdot\boldsymbol{R}_\alpha}$$

$\boldsymbol{P}_{21}(\beta j) = -\gamma_\alpha\Omega_\alpha^2 e^{-j\boldsymbol{G}_j\cdot\boldsymbol{R}_\beta}$, $\boldsymbol{P}_{22}(\alpha\beta) = \gamma_\alpha\Omega_\alpha^2\delta_{\alpha\beta}$, $\boldsymbol{Q}_{11}(ij) = \delta_{ij}$, $\boldsymbol{Q}_{22}(\alpha\beta) = \gamma_\alpha\Omega_\alpha^2\delta_{\alpha\beta}$, the Bloch wave vector $K = [k_x, k_y]$ and the reciprocal lattice vector $\boldsymbol{G} = [G_x, G_y]$. Here, i and j run for the reciprocal vectors and α, β run for resonators in the supercell. Ω^2 is the normalized frequency, γ_α is the normalized mass of the metamaterial thin plate, Ω_α^2 is the normalized resonance frequency of each resonator (see appendix A).

Then, the band diagram calculation for flexural waves is reduced to a generalized eigenvalue problem by sweeping Bloch wave vector in the irreducible Brillouin zone for the frequency f defined as

$$f = \frac{\Omega}{2\pi a}\sqrt{\frac{\rho h}{D}}. \tag{5}$$

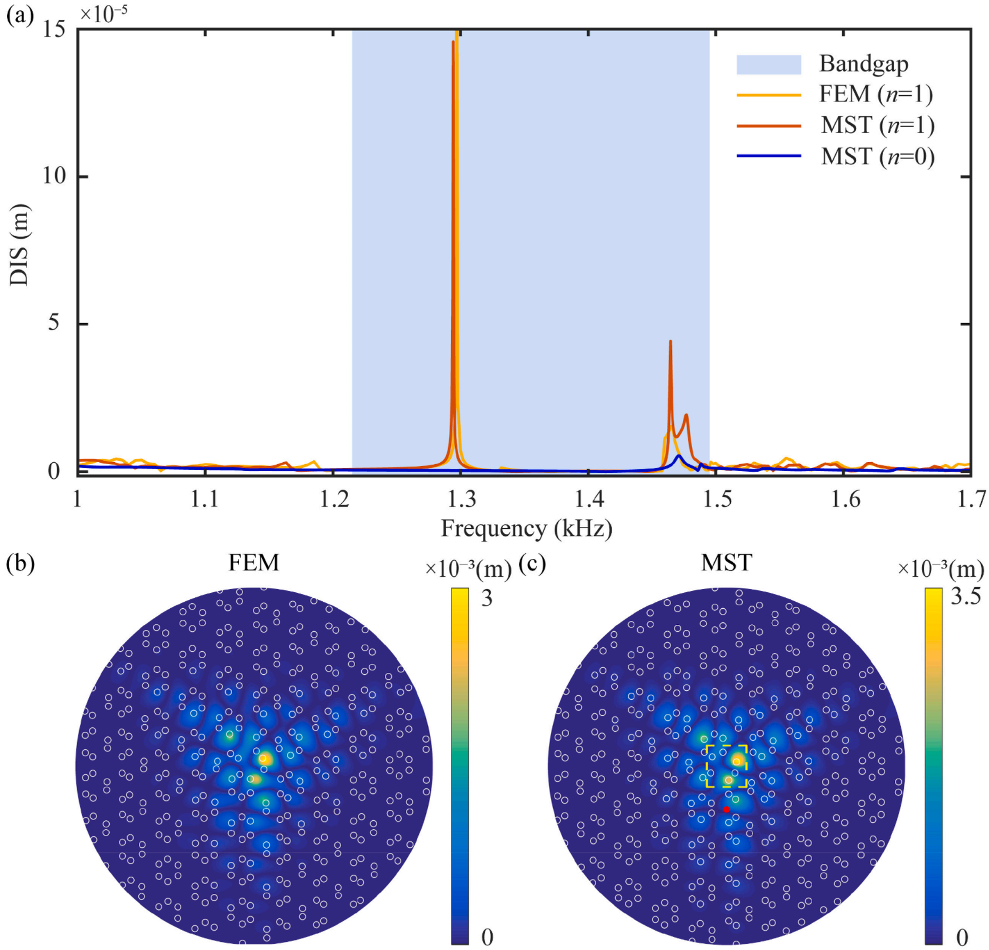

Fig. 3. (a) The out-of-plane displacement measured at the cluster center for both trivial ($n = 0$) and nontrivial ($n = 1$) configurations from the MST and FEM simulations. The shaded background indicates the vortex ($n = 1$) bandgap coming from our PWE prediction. The vibration patterns obtained from (b) MST and (c) FEM simulations when the vortex ($n = 1$) is excited by a point source (red dot) of Dirac frequency. The dashed square in panel (c) illustrates the attached piezoelectric sheet for energy harvesting.

Fig. 2(a) shows the band diagram of flexural waves for the pristine honeycomb lattice whose double Dirac cones appear at the Dirac frequency $f_D = 1294$ Hz at the center of the Brillouin zone. The resonant frequency of all resonators is set as $f_r = 2414.7$ Hz in the computation. The readers of interest are referred to Refs. [51,60] for more information, such as the pseudo-spin wave modes and the relationship between the Dirac frequency and the resonant frequency of the resonators. The double Dirac cones are coming from the zone-folding effect which folds the pair of Dirac cones of the honeycomb lattice to the center of the Brillouin zone. To understand the gap-opening effect of the Kekulé distortion and obtain the common bandgap of the mechanical analogue of Jackiw-Rossi vortex as mentioned in Fig. 1, we evaluate bandgap opening when Kekulé phase varies from 0 to 2π at constant distortion amplitude $\Delta = 0.12a_0$ and exhibit the bandgap variation in Fig. 2(b). When the positions of resonators are distorted, the inversion symmetry of the supercell is broken resulting in the opening of a gap at the double Dirac cone frequency [59]. The blue lines bound the bandgap edges during the phase variation, while the bulk bands at the top and bottom of the band gap are left in blank. From Fig. 2(b), we observe the bandgap has a period of $2\pi/3$, and the dark blue region constitutes the common bandgap of the Kekulé vortex in the frequency range [1215, 1495] Hz. Figures 2(c) and 2(d) display the band structures by PWE and FEM verification when $\phi = 0$ and $\phi = \pi$, respectively. In the FEM verification, we use geometrical parameters and material properties as mentioned at the beginning of Sec. 3. On the other hand, our PWE approach is solely based on flexural waves at low frequencies. The band structures computed from the FEM and PWE methods agree quite well with each other proving the accuracy of the employed methods. Therefore, the full FEM simulation provides a clear support to the validity of the approximate approach based on flexural wave assumption and spring-mass modeling. It should be mentioned that the additional bands emerging in FEM results correspond to shear-horizontal and symmetric Lamb modes, while those modes appearing as flat bands have a local resonance origin [29,51,62].

3.2. Multiple scattering theory

For the mechanical metamaterial with a finite distortion of the honeycomb lattice as per Eq. (1), we use the multiple scattering theory (MST) [60,61,63,64] to calculate flexural wave propagation and further to compute the average harvesting power by a piezoelectric patch. The total incoming wave of each resonator is determined by the scattering field of other resonators and the external point source excitation as (see Appendix B)

$$\psi(\boldsymbol{r}_i) = \psi_0(|\boldsymbol{r}_i - \boldsymbol{R}_{eps}|) + \sum_{num \neq i} T_{num}\Lambda_e(\boldsymbol{R}_{num})\,\boldsymbol{G}_0(|\boldsymbol{r}_i - \boldsymbol{R}_{num}|) \tag{6}$$

where T_{num} is the coefficients of the system, $\boldsymbol{R}_{num} = R(\boldsymbol{R}_{i\alpha})$ runs for all lattice sites, $\boldsymbol{G}_0$ is the Green function (see Appendix B).

Then, the multiple scattering field of the metamaterial thin plates can be written in matrix form as

$$[\boldsymbol{P}]_{num\times num}\begin{bmatrix}\Lambda_e(\boldsymbol{R}_1)\\ \Lambda_e(\boldsymbol{R}_2)\\ \vdots \\ \Lambda_e(\boldsymbol{R}_{num})\end{bmatrix} = \begin{bmatrix} G_0(|\boldsymbol{R}_1 - \boldsymbol{R}_{eps}|)\\ G_0(|\boldsymbol{R}_2 - \boldsymbol{R}_{eps}|)\\ \vdots \\ G_0(|\boldsymbol{R}_{num} - \boldsymbol{R}_{eps}|)\end{bmatrix} \tag{7}$$

where

$$[\boldsymbol{P}] = \begin{bmatrix} 1 & -T_2G_0(|\boldsymbol{R}_1 - \boldsymbol{R}_2|) & \cdots & -T_{num}G_0(|\boldsymbol{R}_1 - \boldsymbol{R}_{num}|)\\ -T_1G_0(|\boldsymbol{R}_2 - \boldsymbol{R}_1|) & 1 & \cdots & -T_{num}G_0(|\boldsymbol{R}_2 - \boldsymbol{R}_{num}|)\\ \vdots & \vdots & \ddots & \vdots \\ -T_1G_0(|\boldsymbol{R}_{num} - \boldsymbol{R}_1|) & -T_2G_0(|\boldsymbol{R}_{num} - \boldsymbol{R}_2|) & \cdots & 1 \end{bmatrix} \tag{8}$$

Eq. (7) is at the heart of the multiple scattering algorithm. On its right side, $G_0(|\boldsymbol{R}_{num} - \boldsymbol{R}_{eps}|)$ characterizes the coupling of each resonator and the point source, where the point source locates at $\boldsymbol{R}_{eps}$. The dimension of the matrix $\boldsymbol{P}$ is *num*. Take a row of the matrix for example, the diagonal coefficient of the square array is 1, corresponding to each resonator. And the others are the coupling effect among different resonators. In short, the scattering field of each resonator is determined by the point source and the field emitted by all the remaining resonators.

In simulations we place a point source at $\boldsymbol{R}_{eps} = [0, -(1+\sqrt{3})R]$ as marked by the red dot in Fig. 3(c), and the topological metamaterial plate consists of a circular cluster of resonators with $|\boldsymbol{R}_{num}| \leqslant Rd$ (Rd is the radius of the cluster). The out-of-plane displacement (DIS) response spectra at the vortex center are calculated with the aforementioned MST algorithm for vortices $n = 1$ and $n = 0$, respectively as shown in Fig. 3 (a). The sharp peak appearing exactly at the Dirac frequency is the fingerprint of the topological bound state. Here, we expect to achieve high-efficient energy harvesting with strong robustness by such a design. Near the upper edge of the common bandgap (highlighted with shaded color) in Fig. 3(a), two additional topologically trivial peaks emerge which can also be good candidates for energy harvesting, though less robust, if one desires their broadband features. For the trivial configuration $n = 0$, the Kekulé distortion leads to shrunken or expanded supercells only, but cannot form a vortex of phase winding, failing to support the topological states at Dirac frequency.

To verify the accuracy of our MST algorithm, we establish a full-scale FEM model to simulate the out-of-plane response spectrum in the finite structure where the boundaries are surrounded by a ring-shaped perfectly matched layer (PML) to avoid unwanted reflections (see Appendix C). As shown in Fig. 3(a), the out-of-plane displacement (DIS) response spectra of the MST and the corresponding FEM verification are highly consistent near the Dirac frequency $f_D = 1294$ Hz, with nearly negligible difference for the two peaks. The out-of-plane displacement fields at the peak's frequency in Fig. 3(b) and (c) are calculated by the FEM and the MST approaches, respectively, showing exactly the same vibration patterns of the topological bound states.

3.3. Piezoelectric response for energy harvesting

We attach a square piezoelectric ceramic transducer (PZT-5H) patch with a side length $L = 42$ mm and thickness $t = 0.1$ mm to the opposite surface of the plate whose position is marked as the dashed yellow square and build the piezoelectric model together with the MST method [see Fig. 3(c)]. Compared with the thin aluminum plate, the piezoelectric patch is thin enough, and its binding contribution to the vibration of the thin plate is relatively weak, so that only slightly affects the vibration amplitude of the thin plate. Therefore, the coupling effect of them on the bound state is ignored. Here, the anisotropic piezoelectric ceramic is also considered as a homogeneous thin plate, whose elastic strain is defined as

$$S_{xx} = -z\frac{\partial^2 w}{\partial x^2};\, S_{yy} = -z\frac{\partial^2 w}{\partial y^2};\, S_{xy} = -z\frac{\partial^2 w}{\partial x\partial y}, \tag{9}$$

where w is the out-of-plane displacement of the thin plate that can be numerically solved by the multiple scattering algorithm.

The electrical displacement along the x and y direction is zero based on the basic assumption of the elastic thin plate [18]. Thereby, we can define the electrical displacement along the out-of-plane direction as

$$D_z = \varepsilon_{33}E_z + e_{31}S_{xx} + e_{32}S_{yy} + e_{36}S_{xy} \tag{10}$$

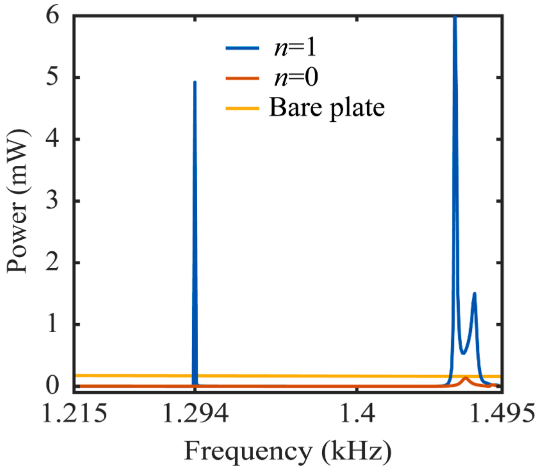

Fig. 4. Variation of the average harvesting power against the excitation frequency for the trivial ($n = 0$) and nontrivial ($n = 1$) clusters. The frequency axis is truncated within the bandgap. A bare plate without any resonators is considered for comparison.

where $\varepsilon_{33} = 1433.6 \quad \varepsilon_0$ is the dielectric permittivity with ε_0 being the vacuum permittivity, E_z is the electric field, and e_{3i} are the piezoelectric ceramic constants.

In this work, the electrical field is uniform along the z-direction, and then, the electrical voltage is given by $V = -tE_z$ and the charge on the PZT surface is $Q = \int_A D_Z dA$. Therefore, the charge variation can be obtained by combining the Eqs. (9) and (10) with the above assumptions as

$$Q = \Theta - L^2 \frac{\varepsilon_{33} V}{t} \tag{11}$$

where $t = 0.1 \quad$ mm is the thickness of the PZT layer, $A = L^2$ is the area of the PZT patch, and Θ is defined as

$$\Theta = -\frac{h}{2} \int_A (e_{31} \frac{\partial^2 w}{\partial x^2} + e_{32} \frac{\partial^2 w}{\partial y^2}) dA \tag{12}$$

The partial derivatives in the integrand can be expanded by Taylor series in the form as

$$\begin{cases} \dfrac{\partial^2 w}{\partial x^2} = \dfrac{w(x_i + \Delta L, y_i) - 2w(x_i, y_i) + w(x_i - \Delta L, y_i)}{\Delta L^2} \\ \dfrac{\partial^2 w}{\partial y^2} = \dfrac{w(x_i, y_i + \Delta L) - 2w(x_i, y_i) + w(x_i, y_i - \Delta L)}{\Delta L^2} \end{cases} \tag{13}$$

where the higher order infinitesimal can be omitted when the incremental step ΔL is enough small.

Substituting Eq. (13) into Eq. (12), Θ can be directly defined as the integral of the displacement w. Therefore, we can get the value of the Θ directly from numerical integration. It is reasonable to treat the PZT patch as a current source in an AC electrical circuit with a defined resistance $R_0 = 1.2 \quad \mathrm{k}\Omega$. The amplitude of the current is given by $I = \omega Q$. Therefore, the amplitude of the current in the AC electrical circuit can be written as

$$I = \frac{\omega |\Theta|}{1 + \omega \varepsilon_{33} R_0 A / t} \tag{14}$$

We therefore arrive to the equation to compute the average harvesting power [18]

$$P = \frac{1}{2} I^2 R_0 = \frac{\omega^2 R_0 |\Theta|^2}{2(1 + \omega \varepsilon_{33} R_0 A / t)^2} \tag{15}$$

In the following sections, we will use the MST method and the piezoelectric power formulated in Eq. (15) to investigate the energy harvesting performance of the topological vortex.

4. Energy harvesting with topological cavities

The energy harvesting performance of the mechanical metamaterial thin plates are our primary objective. We use the MST method together with piezoelectric theory to study the influence of the distortion amplitude A_i and the vortex radius $\boldsymbol{\xi}_i$ on the energy harvesting performances of the mechanical metamaterial thin plates.

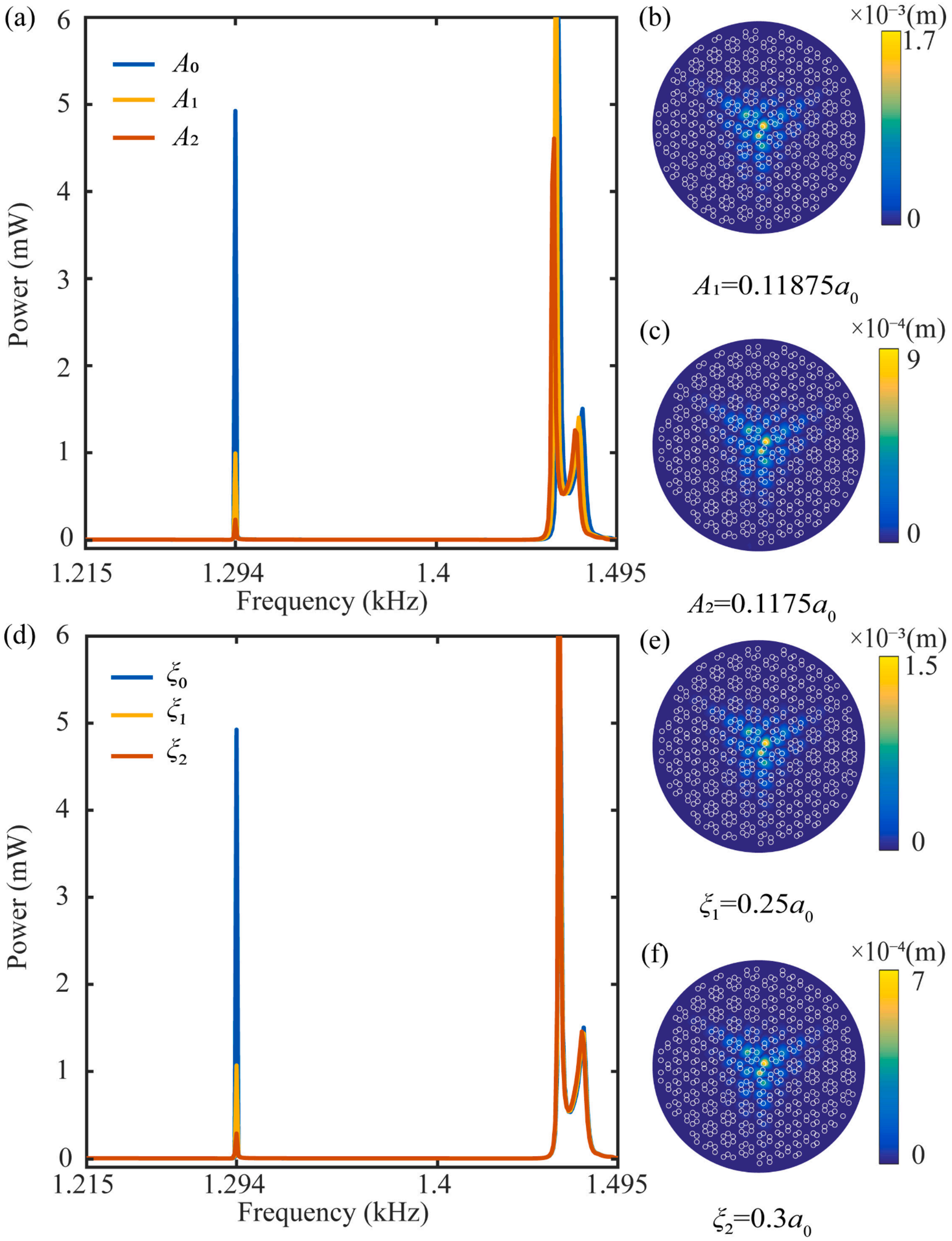

Fig. 5. (a) Power spectra for elastic energy harvesting modulated by the distortion amplitude A_i and the out-of-plane displacement fields with distortion amplitudes (b) $A_1 = 0.11875a_0$ and (c) $A_2 = 0.1175a_0$, respectively. (d) Response spectra of output average power for energy harvesting regulated by the vortex radius ξ_i and the out-of-plane displacement fields with vortex radii (e) $\xi_1 = 0.25\ a_0$ and (f) $\xi_2 = 0.3\ a_0$, respectively.

Figure 4 shows the output average power P of electrical energy harvesting in the metamaterial plates with the finite vorticity $n = 1$ and $n = 0$, as shown by the blue and red lines, respectively. For reference, we also calculate the power for a bare plate. If not specified, the locations of the point source and the PZT layer remain unchanged as indicated in Fig. 3(c), respectively. For the trivial lattice ($n = 0$), we observe that at the Dirac frequency the response spectra of the output power do not capture a peak, remaining at a quasi-zero level since vibrations are almost prohibited by the bandgap. This is understandable given that the trivial lattice does not embody a phase winding process, therefore does not support any topological bound states in the bandgap. For the topological vortex ($n = 1$), the output power spectra, like that of the flexural wave response at the vortex core in Fig. 3(a), accurately capture a peak power about 4.93 mW at the Dirac frequency. It can also be found that two peaks appear close to the upper limit of the common bandgap resulting from the conventional localized modes as shown in Fig. 3(a). Among the two peaks, one even gains a higher output power than that at the Dirac frequency although the displacement amplitude in Fig.3(a) is smaller. This can be explained by Eq. (12) since the electric power

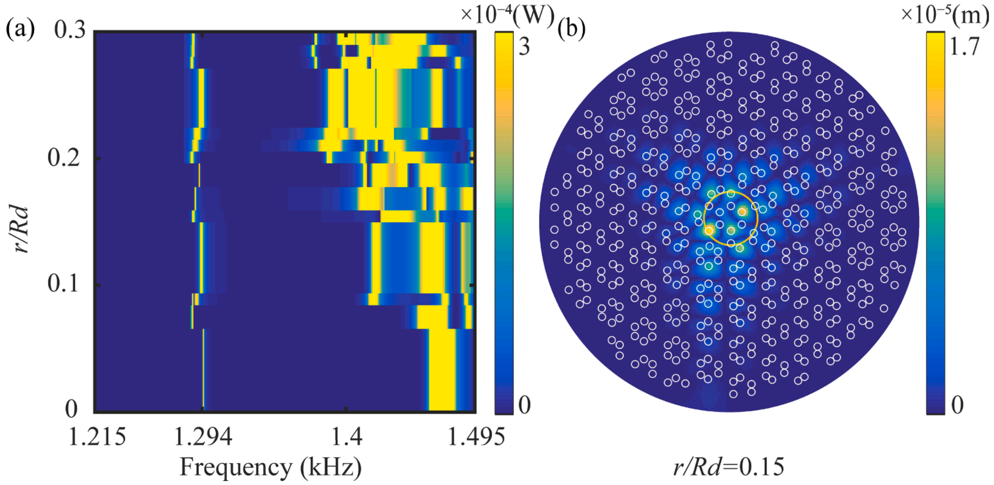

Fig. 6. (a) Color maps showing the level of harvesting power spectra when symmetry-preserving defects are introduced at the vortex core. As illustrated in panel (b), the resonators inside the yellow circle (of radius r) are moving back to their primitive honeycomb sites. The flexural wave pattern is shown for one particular defect ratio r=0.15Rd with Rd being the radius of the whole cluster.

is related to the elastic strain of the plate rather than to the amplitude of displacement. In addition, we plot the piezoelectric response spectrum of the bare plate without any resonator as depicted by the yellow line, which possesses a stable output power about 0.17 mW. The peak value of the output power induced by the topological bound state is about 30 times higher than that of a bare plate, showing a remarkable enhancement. In stark contrast, the power level for $n = 0$ around the Dirac frequency is only 0.9% of that of the bare plate owing to the existence of the bandgap.

In Fig. 5, we study how the distortion amplitude A_i and the vortex radius ξ_i affect the piezoelectric power spectra. In Fig. 5(a), we consider a series of distortion amplitude $A_0 = 0.12a_0$, $A_1 = 0.11875a_0$ and $A_2 = 0.1175a_0$ to evaluate their effects on the power spectra. With the decrease of the distortion amplitude, the amplitude of output power P induced by the topological bound state also decreases gradually while its peak frequency remains pinned to the Dirac frequency $f_D = 1294$ Hz. Since the topological bound states for these three scenarios have very similar wave patterns as seen in Figs. 3(c), 5(b) and 5(c), the decrease in vibrating amplitude also leads to a decrease in strain value that explains the behavior of the power peak's evolution. On the other hand, the frequency of the topological power peak is determined by the undistorted honeycomb lattice, fixed at the Dirac frequency, and is not easily affected by the distortion amplitude A_i.

The effect of the vortex radius on the power spectra is shown in Fig. 5(d). We select a set of vortex radii $\xi_0 = 0.1a_0$, $\xi_1 = 0.25a_0$ and $\xi_2 = 0.3 \quad a_0$ to study their effects on the output power spectra. Contrary to the trend shown in Fig. 5(a), the amplitude of P at the topological peak decreases gradually with the increasing vortex radius, meanwhile its corresponding frequency remains firmly pinned to the Dirac frequency. This difference is understandable because of the Kekulé distortion function $\Delta(\boldsymbol{r}_{i\alpha}) = A_0 tanh(|\boldsymbol{r}_{i\alpha}|/\xi_0)$ as discussed in Sec. 2, since the vortex radius ξ_i is inversely correlated with the Kekulé distortion $\Delta(\boldsymbol{R}_{i\alpha})$. Likewise, from Fig. 3(c), Figs. 5(e) and 5(f), we see the maximum value of the displacement fields gradually decreases with the increase of the vortex radius ξ_i while the field distribution keeps unchanged, and then the amplitude of output power P will decrease due to the reduction of second derivative in Eq. (12).

We now examine the harvesting power resulting from the localized modes near the upper edge of the band gap. These two peaks belong to high-order trivial cavity modes since they can be shifted into the continuum of bulk bands [42,43]. The main peak values do not follow a monotonous behavior with the decrease of the distortion amplitude or the increase of the vortex radius. Besides, the peaks of the power spectra at the upper edge of the band gap also experience a spectral shifting. Comparing the topological and trivial bound states induced power peaks, we conclude that: 1) the topological peak is more stable in frequency and has high quality factor which is promising for sensing application; 2) the behavior of topological peak is predictable making it more feasible and controllable in functional design.

5. Robustness study of topological cavities

In this section, we systematically study the robustness of power peaks in the metamaterial thin plates against both symmetry-preserving and symmetry-breaking defects. The symmetry-preserving defects will not shift the Dirac frequency of the system, and thus satisfy the particle-hole symmetry that is required to protect the related topological states. On the contrary, the symmetry-breaking defects are rather casual, for instance, resonators with random resonant frequency shifting [65]. Detailed information is presented and discussed below.

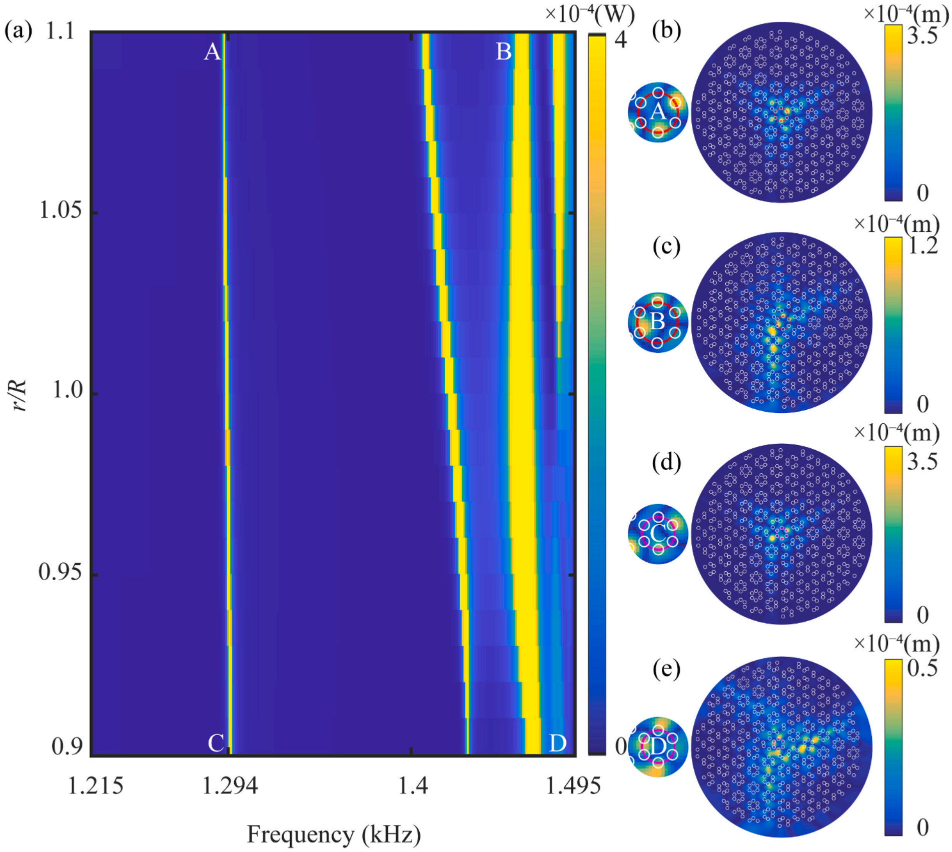

Fig. 7. (a) Power map for another symmetry-preserving defect, similar to Fig. 6, here the vortex is perturbed by shrinking or expanding the six central resonators away from the primitive honeycomb lattice sites. The radiation patterns of the topological state when the six resonators are (b) expanded at the point A or (d) shrunken at the point C by 10% relative to the initial position R. The field patterns for the third peak when the six resonators are (c) expanded at the point B or (e) shrunken at the point D by10% relative to the initial position R.

5.1. Symmetry-preserving defects

For the symmetry-preserving defects we first investigate the evolution of the output average power P with the symmetry defect ratio r/Rd, where r and Rd are the radii of defect area and cluster, respectively. The defects are introduced by moving the resonators within the defect area [see the yellow circle in Fig. 6(b)] back to the primitive honeycomb arrangement without the Kekulé distortion ($\Delta = 0$ inside the defect area). We gradually increase the defect ratio up to 0.3, and plot the corresponding spectra of the harvesting power P in Fig. 6(a). For the topological peak, the frequency undergoes a slight perturbation around the Dirac frequency $f_D = 1294$ Hz, showing only 0.62% spectral shifting even when the perturbation is increased to an extremely high level of $r/Rd = 0.3$. The reason for the strong robustness of the topological bound state is that the structural Dirac frequency of the defect is still consistent with that of the Kekulé distorted vortex, thus preserving the particle-hole symmetry. Figure 6(b) depicts the flexural wave field of topological bound state for $r/Rd = 0.15$, revealing that the flexural wave is still confined in the vortex core but now allowing more energy penetration into the crystal bulk. Different from the topological peak, the trivial power peaks show poorer robustness. Beyond the evident spectral shifting, there appear some random peaks of high uncertainty. This behavior results from the fact that for each symmetric-breaking defect, we are dealing with new structural configurations that induce rather casual trivial modes due to the complex coupling effects.

Fig. 7 shows the evolution process of the output power P for another symmetry-preserving defect, namely when the six resonators around the vortex center are arranged as a hexagon which endures location expanding or shrinking in comparison to the primitive honeycomb lattice. The output power P induced by the topological bound state shows excellent robustness both in frequency and amplitude. Specifically, there is only a maximum 0.15% frequency fluctuation (corresponding to 2 Hz) when the resonators shrink or expand by 10%. The robustness of the topological power peak can again be explained by the fact that such defect is symmetrical at the Dirac frequency. With the perturbation of six resonators at the vortex core, there appears obvious frequency shifts and new peaks caused by trivial localized modes. We further display the out-of-plane displacement fields at A-D points in Fig. 7(b)-(e), respectively. It can be observed that the topological bound states at A [Fig. 7(b)] and C [Fig. 7(d)] points almost share the same radiation pattern as the undistorted case in Fig. 3(c). However, the radiation patterns at B [Fig. 7(c)] and D [Fig. 7(e)] points are totally different, both presenting large energy leakages into the crystal bulk especially along the three directions of narrowest bandgap, as depicted in Fig. 1

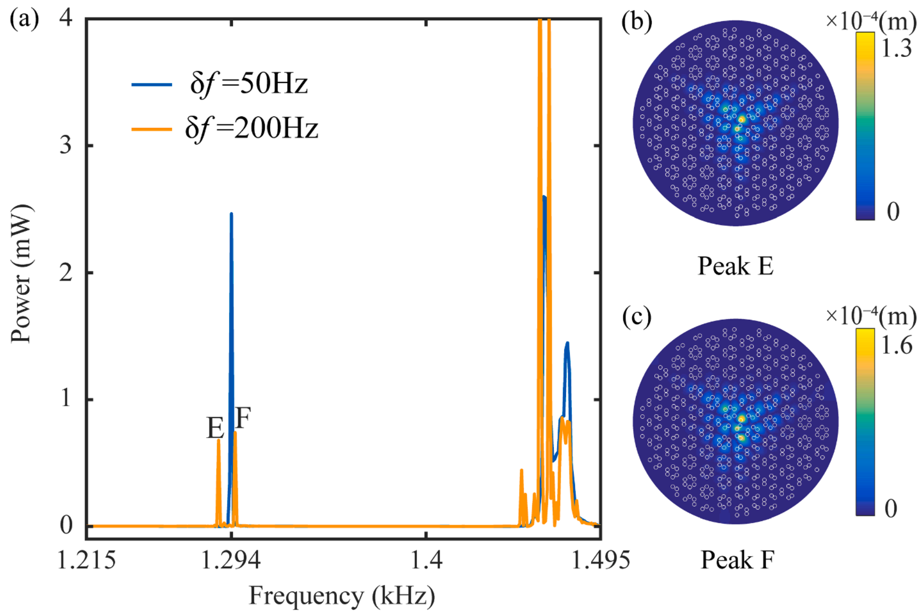

Fig. 8. (a) Response spectra of the output power P in non-trivial Kekulé cluster of resonators modulated by a random distribution of the frequencies of the six resonators around the vortex center, with a maximum deviation frequency δf. The topological peak of the output power and the bound states of displacement field for (b) peak E and (c) peak F at Dirac frequency show strong robustness even when δf reaches 200 Hz. On the other hand, when increasing δf to 200Hz, the disorder produces two new localized states E and F.

and Fig. 2(b). Such uncertainty and weak confinement make the trivial localized modes less useful although the induced power peaks at B and D have high values and relatively broadband property.

5.2. Symmetry-breaking defects

There are many choices for the symmetry-breaking defects that lead to a spectral shift from Dirac frequency, such as geometrical defects resulting from a perturbation in the height and the diameter of the resonator's neck and head, or slight variations of material parameters [65]. Overall, the above-mentioned defects will mainly affect the resonant frequency. The vortex core is of particular significance for the topological state, hence is more vulnerable to such random defects. In this context, we study the influence of the symmetry-breaking defects by introducing a random distribution of the resonant frequencies for the six resonators nearest to the center. The randomness obeys a uniform distribution with maximum deviation δf. As depicted in Fig. 8, for one typical disturbed system when $\delta f = 50$ Hz, the topological power peak [see Fig. 8(a)] conserves a single peak at the Dirac frequency $f_D = 1294$ Hz, but with a decrease in the power peak's amplitude as compared to the undistorted case in Fig. 4. When the random frequency disturbance is increased to the maximum value $\delta f = 200$ Hz (normalized deviation ratio $\delta f / f_D = 0.155$), the topological power peak splits into two peaks E and F, nevertheless the frequency shift is still within 5 Hz. We exhibit the displacement fields at peaks E and F in Figs. 8(b) and 8(c), respectively. Given that the six centered resonators have different frequency shifts (as asymmetric defect) with the same max δf, it is possible to induce multiple peaks around the original Dirac frequency. From the fields displayed in Fig. 8(b) and (c), one can find that the two radiation patterns are very similar to the one without distortion in Fig. 3(c). The two splitting peaks E and F are the result of hybridization process between the topological mode and the trivial defect mode caused by frequency disorders. For the trivial localized modes at higher frequencies, they evolve into complex profiles due to randomness.

6. Conclusion

An energy harvesting system based on the topological cavity in phononic thin plate is designed and evaluated by theoretical calculation and FEM verification. The topological cavities are constructed at the center of the phononic crystals by mimicking the Jackiw-Rossi binding mechanism with Kekulé modulation. We consider a hexagonal lattice with spatially uniform distortion amplitude and Kekulé phase to study the distortion induced band gap opening process by means of the PWE method, and find the common bandgap of the aperiodic lattice. The bandgap width is exactly zero at the vortex center. This is very useful for the design of a topologically protected device for elastic energy harvesting. The output power is computed by a combination of the MST and piezoelectric harvesting algorithm. The harvesting power induced by the topological bound state is about 30 times that of the bare plate. The distortion amplitude and the vortex radius of the Kekulé distortion only modulate the peak values of the topological peaks but will not shift the peak from the Dirac frequency. The robustness study shows that the output average power of the phononic plates can resist to both the symmetry-preserving and symmetry-breaking defects at moderate disorder level. Beyond the energy harvesting functionality, we expect this topological cavity will offer a robust solution for practical applications like sensing, signal processing and structural health monitoring, etc.

CRediT authorship contribution statement

Zhihui Wen: Methodology, Software, Validation, Investigation, Writing - original draft, Writing - review & editing, Visualization. **Yabin Jin:** Supervision, Conceptualization, Investigation, Resources, Writing - original draft, Writing - review & editing, Visualization, Project administration, Funding acquisition. **Penglin Gao:** Supervision, Conceptualization, Methodology, Software, Investigation, Writing - original draft, Writing - review & editing, Visualization. **Xiaoying Zhuang:** Supervision, Software, Methodology, Visualization, Writing - original draft, Writing - review & editing. **Timon Rabczuk:** Supervision, Writing - original draft, Writing - review & editing. **Bahram Djafari-Rouhani:** Supervision, Writing - original draft, Writing - review & editing.

Declaration of Competing Interest

The authors declare that they have no known competing financial interests or personal relationships that could have appeared to influence the work reported in this paper.

Acknowledgments

This work is supported by the National Natural Science Foundation of China (11902223), the Shanghai Pujiang Program (19PJ1410100), the program for professor of special appointment (Eastern Scholar) at Shanghai Institutions of Higher Learning, the Fundamental Research Funds for the Central Universities, Shanghai municipal peak discipline program (2019010106) and the High-Level Foreign Expert Program of Tongji University.

Appendix A. . Derivation of the plane wave expansion

The waves propagating in periodic systems can be written as Floquet-Bloch waves,

$$w(\boldsymbol{r}) = \sum_{\boldsymbol{G}} w(\boldsymbol{G}) \quad e^{-j(\boldsymbol{G}+\boldsymbol{K})\cdot\boldsymbol{r}}, \tag{16}$$

where $\boldsymbol{K}$ denotes the Bloch wave vector and $\boldsymbol{G} = b\boldsymbol{g}_1 + d\boldsymbol{g}_2$ the reciprocal lattice vector. In the reciprocal lattice, b and d are integers, $\boldsymbol{g}_1$ and $\boldsymbol{g}_2$ are the basis vectors of the reciprocal lattice with $\boldsymbol{a}_i \cdot \boldsymbol{g}_j = 2\pi\delta_{ij}(i,j = 1,2.)$, where $\boldsymbol{a}_i$ denote the honeycomb lattice vectors.

Using Floquet-Bloch theorem from Eq. (16) for the mechanical metamaterial plate in Eq. (2) and the resonators in Eq. (3), we acquire

$$\begin{aligned} &S\left(D\left((\boldsymbol{k}_x + \boldsymbol{G}_x)^2 + (\boldsymbol{k}_y + \boldsymbol{G}_y)^2\right)^2 - \omega^2 \rho h\right) w(\boldsymbol{G}) = \\ &\sum_{\alpha} k_n \left(w_1(\boldsymbol{R}_\alpha) - \sum_{\boldsymbol{G}'} w(\boldsymbol{G}') \quad e^{-j(\boldsymbol{G}'+\boldsymbol{K})\cdot\boldsymbol{R}_\alpha} \right) \quad e^{j(\boldsymbol{G}+\boldsymbol{K})\cdot\boldsymbol{R}_\alpha}, \end{aligned} \tag{17}$$

where $S = \sqrt{3}a^2/2$ is the area of the supercell, $K = [k_x, k_y]$ and $\boldsymbol{G} = [G_x, G_y]$. Periodic boundary conditions of resonators in the unit cell implied by Floquet-Bloch theorem can be written as

$$w_1(\boldsymbol{R}_\alpha) = w_1(\boldsymbol{0}_\alpha) \quad e^{-j\boldsymbol{K}\cdot\boldsymbol{R}_\alpha} \tag{18}$$

where $w_1(\boldsymbol{0}_\alpha)$ is the Bloch displacement of the resonator α in the reference supercell. Substituting Eq. (18) into Eqs. (17) and (3), we can obtain the following equations

$$\begin{aligned} &\left(\left((\boldsymbol{k}_x + \boldsymbol{G}_x)^2 + (\boldsymbol{k}_y + \boldsymbol{G}_y)^2\right)^2 a^4 - \Omega^2\right) w(\boldsymbol{G}) = \\ &\sum_{\alpha} \gamma_\alpha \Omega_\alpha^2 \left(w_1(\boldsymbol{0}_\alpha) - \sum_{\boldsymbol{G}'} w(\boldsymbol{G}') \quad e^{-j(\boldsymbol{G}'+\boldsymbol{K})\cdot\boldsymbol{R}_\alpha} \right) \quad e^{j\boldsymbol{G}\cdot\boldsymbol{R}_\alpha}; \end{aligned} \tag{19}$$

$$-\Omega^2 w_1(\boldsymbol{0}_\alpha) = \Omega_\alpha^2 \left(\sum_{\boldsymbol{G}} w(\boldsymbol{G}) \quad e^{-j\boldsymbol{G}\cdot\boldsymbol{R}_\alpha} - w_1(\boldsymbol{0}_\alpha) \right), \tag{20}$$

where $\Omega^2 = \omega^2 \rho a^2 h / D$ is the normalized frequency, $\gamma = m_R/(\rho S h)$ the normalized mass of the system, $\Omega_\alpha^2 = k_n \rho a^2 h / m_n D$ the normalized resonance frequency of each resonator.

Appendix B. . Derivation of the multiple scattering theory

By some algebraic substitution and using Eqs. (17) and (3), the equation of motion can be written as [60]

$$\left(\nabla^4 - \omega^2\rho h/D\right)w(\boldsymbol{r}) = \sum_{num} t_{num} w_1(\boldsymbol{R}_{num})\delta(\boldsymbol{r} - \boldsymbol{R}_{num}), \tag{21}$$

where $\boldsymbol{R}_{num} = R(\boldsymbol{R}_{i\alpha})$ runs for all lattice sites. The stiffness coefficient is

$$t_{num} = \frac{\gamma_{num} S(\Omega a)^2}{a^4\left(1 - (\Omega a)^2/(\Omega_{num} a)^2\right)} \tag{22}$$

where Ω, γ_{num}, Ω_{num} and S are the normalized quantities as defined in Sec. 3.1, num denotes the index of resonators attached on the plate.

Here, the Green function G_0 is used to investigate the flexural modes of the metamaterial thin plates, and we rewrite Eq. (11) as [60]

$$\left(\nabla^4 - \Omega^2/a^2\right)G_0(|\boldsymbol{r}|) = \delta(|\boldsymbol{r}|) \tag{23}$$

In the derivation, the resonators are treated as punctual sources. The scattering fields and point source excitation of each resonator can be defined by Green function. The Green function is defined by the zeroth-order Hankel function and the modified Bessel function of the second kind. The Bessel function is singular at $|r| = 0$. Therefore, we need to define the case of $|r| = 0$ for the Green function as follows.

$$G_0(|\boldsymbol{r}|) = \begin{cases} \dfrac{j}{8k^2}\left[H_0(k|\boldsymbol{r}|) + \dfrac{2j}{\pi}K_0(k|\boldsymbol{r}|)\right] & |\boldsymbol{r}| \neq 0; \\ \dfrac{j}{8k^2} & |\boldsymbol{r}| = 0, \end{cases} \tag{24}$$

where $k = \sqrt[4]{(2\pi f)^2(\rho h)/D}$ is the wave number and f is the working frequency.

The solution of the flexural wave modes [60] can be therefore defined as

$$w(\boldsymbol{r}) = \psi_0\left(|\boldsymbol{r} - \boldsymbol{R}_{eps}|\right) + \sum_{num} T_{num}\Lambda_e(\boldsymbol{R}_{num})\ \boldsymbol{G}_0(|\boldsymbol{r} - \boldsymbol{R}_{num}|) \tag{25}$$

From Eq. (15) we see the flexural waves in the plate are determined by the external excitation $\psi_0\left(|\boldsymbol{r} - \boldsymbol{R}_{eps}|\right) = G_0\left(|\boldsymbol{r} - \boldsymbol{R}_{eps}|\right)$ and the scattering of all the resonators, $\boldsymbol{R}_{eps}$ denotes the position of the external excitation and $\Lambda_e(\boldsymbol{R}_{num})$ is the scattering coefficients of the resonator located at $\boldsymbol{R}_{num}$ when excited by an external punctual source. The coefficients T_{num} of the system can be denoted as [60]

$$T_{num} = \frac{t_{num}}{1 - jt_{num}/(8k^2)} \tag{26}$$

Here, we use the Green function as defined in Eq. (24).

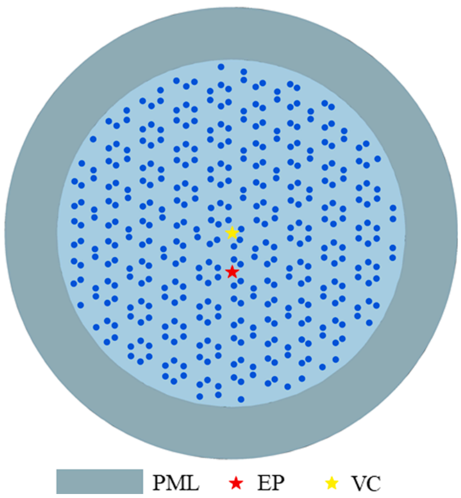

Fig. 9. The 3D modeling of Jackiw-Rossi vortex in phononic plate. The red and yellow stars represent the excitation point (EP) and vortex center (VC), respectively. The phononic cluster is surrounded by a PML to mimic infinite space.

Appendix C. . Finite element modeling

We establish a full-scale 3D model in thin plate that contains a topological vortex (see Fig. 9) to simulate the mechanical response as studied in Fig. 3. For FEM calculations, we use free tetrahedral elements to mesh the 3D model. The meshing contains about 3 million elements with about 120 million degrees of freedom for solving in COMSOL. A ring-shaped perfectly matched layer is surrounding the calculation domain to avoid reflection at the boundary. The star symbols represent the excitation source (red) and the vortex center (yellow).

References

[1] S. Timorian, M. Ouisse, N. Bouhaddi, S. De Rosa, F. Franco, Numerical investigations and experimental measurements on the structural dynamic behaviour of quasi-periodic meta-materials, Mech. Syst. Sig. Process. 136 (2020), 106516.
[2] M. Gupta, M. Ruzzene, Dynamics of quasiperiodic beams, Crystals 10 (2020) 1144.
[3] G. Ma, P. Sheng, Acoustic metamaterials: from local resonances to broad horizons, Sci. Adv. 2 (2016), e1501595.
[4] Y. Jin, Y. Pennec, B. Bonello, H. Honarvar, L. Dobrzynski, B. Djafari-Rouhani, M. Hussein, Physics of surface vibrational resonances: Pillared phononic crystals, metamaterials, and metasurfaces, Rep. Prog. Phys. (2021), https://doi.org/10.1088/1361-6633/abdab8.
[5] S.Y. Ren, Y.-C. Chang, Theory of confinement effects in finite one-dimensional phononic crystals, Physical Review B 75 (2007), 212301.
[6] Y. Jin, D. Torrent, B. Djafari-Rouhani, Robustness of conventional and topologically protected edge states in phononic crystal plates, Physical Review B 98 (5) (2018) 054307.
[7] Y. Chen, L. Wang, Multiband wave filtering and waveguiding in bio-inspired hierarchical composites, Extreme Mech. Lett. 5 (2015) 18–24.
[8] Y. Jin, N. Fernez, Y. Pennec, B. Bonello, R.P. Moiseyenko, S. Hémon, Y. Pan, B. Djafari-Rouhani, Tunable waveguide and cavity in a phononic crystal plate by controlling whispering-gallery modes in hollow pillars, Physical Review B 93 (5) (2016) 054109.
[9] A. Colombi, P. Roux, M. Rupin, Sub-wavelength energy trapping of elastic waves in a metamaterial, J Acoust Soc Am 136 (2) (2014) EL192–EL198.
[10] Y. Jin, B. Djafari-Rouhani, D. Torrent, Gradient index phononic crystals and metamaterials, Nanophotonics, 8 (2019) 685.
[11] J. Hyun, W. Choi, M. Kim, Gradient-index phononic crystals for highly dense flexural energy harvesting, Appl. Phys. Lett. 115 (2019), 173901.
[12] C.-S. Park, Y.C. Shin, S.-H. Jo, H. Yoon, W. Choi, B.D. Youn, M. Kim, Two-dimensional octagonal phononic crystals for highly dense piezoelectric energy harvesting, Nano Energy 57 (2019) 327–337.
[13] F. Liu, A. Phipps, S. Horowitz, K. Ngo, L. Cattafesta, T. Nishida, M. Sheplak, Acoustic energy harvesting using an electromechanical Helmholtz resonator, J Acoust Soc Am 123 (2008) 1983–1990.
[14] W.-C. Wang, L.-Y. Wu, L.-W. Chen, C.-M. Liu, Acoustic energy harvesting by piezoelectric curved beams in the cavity of a sonic crystal, Smart Mater. Struct. 19 (2010), 045016.
[15] S. Qi, M. Oudich, Y. Li, B. Assouar, Acoustic energy harvesting based on a planar acoustic metamaterial, Appl. Phys. Lett. 108 (2016), 263501.
[16] J.M. De Ponti, A. Colombi, R. Ardito, F. Braghin, A. Corigliano, R.V. Craster, Graded elastic metasurface for enhanced energy harvesting, New J. Phys. 22 (2020), 013013.
[17] Z. Chen, Y. Xia, J. He, Y. Xiong, G. Wang, Elastic-electro-mechanical modeling and analysis of piezoelectric metamaterial plate with a self-powered synchronized charge extraction circuit for vibration energy harvesting, Mech. Syst. Sig. Process. 143 (2020), 106824.
[18] M. Oudich, Y. Li, Tunable sub-wavelength acoustic energy harvesting with a metamaterial plate, J. Phys. D Appl. Phys. 50 (2017), 315104.
[19] M.I. Hussein, C.N. Tsai, H. Honarvar, Thermal conductivity reduction in a nanophononic metamaterial versus a nanophononic crystal: a review and comparative analysis, Adv. Funct. Mater. 30 (2019) 1906718.
[20] H. Ji, Y. Liang, J. Qiu, L. Cheng, Y. Wu, Enhancement of vibration based energy harvesting using compound acoustic black holes, Mech. Syst. Sig. Process. 132 (2019) 441–456.
[21] G. Hu, J. Wang, L. Tang, A comb-like beam based piezoelectric system for galloping energy harvesting, Mech. Syst. Sig. Process. 150 (2021), 107301.
[22] Z. Wang, T. Li, A semi-analytical model for energy harvesting of flexural wave propagation on thin plates by piezoelectric composite beam resonators, Mech. Syst. Sig. Process. 147 (2021), 107137.
[23] Y. Jin, B. Bonello, R.P. Moiseyenko, Y. Pennec, O. Boyko, B. Djafari-Rouhani, Pillar-type acoustic metasurface, Physical Review B 96 (2017), 104311.
[24] S.-H. Jo, H. Yoon, Y.C. Shin, M. Kim, B.D. Youn, Elastic wave localization and harvesting using double defect modes of a phononic crystal, J. Appl. Phys. 127 (2020), 164901.
[25] S.-H. Jo, H. Yoon, Y.C. Shin, W. Choi, C.-S. Park, M. Kim, B.D. Youn, Designing a phononic crystal with a defect for energy localization and harvesting: Supercell size and defect location, Int. J. Mech. Sci. 179 (2020) 105670.
[26] A.T. Fabro, H. Meng, D. Chronopoulos, Uncertainties in the attenuation performance of a multi-frequency metastructure from additive manufacturing, Mech. Syst. Sig. Process. 138 (2020) 106557.
[27] G. Ma, M. Xiao, C.T. Chan, Topological phases in acoustic and mechanical systems, Nature Reviews Physics 1 (4) (2019) 281–294.
[28] Z. Yang, F. Gao, X. Shi, X. Lin, Z. Gao, Y. Chong, B. Zhang, Topological acoustics, Phys. Rev. Lett. 114 (11) (2015) 114301.
[29] Y. Jin, W. Wang, Z. Wen, D. Torrent, B. Djafari-Rouhani, Topological states in twisted pillared phononic plates, Extreme Mech. Lett. 39 (2020) 100777.
[30] W. Wang, Y. Jin, W. Wang, B. Bonello, B. Djafari-Rouhani, R. Fleury, Robust Fano resonance in a topological mechanical beam, Physical Review B 101 (2) (2020) 024101.
[31] C. He, X. Ni, H. Ge, X.-C. Sun, Y.-B. Chen, M.-H. Lu, X.-P. Liu, Y.-F. Chen, Acoustic topological insulator and robust one-way sound transport, Nat. Phys. 12 (2016) 1124–1129.
[32] Y. Jin, W. Wang, B. Djafari-Rouhani, Asymmetric topological state in an elastic beam based on symmetry principle, Int. J. Mech. Sci. 186 (2020), 105897.
[33] Y. Chen, F. Meng, X. Huang, Creating acoustic topological insulators through topology optimization, Mech. Syst. Sig. Process. 146 (2021), 107054.
[34] P. Gao, Z. Zhang, J. Christensen, Sonic valley-Chern insulators, Physical Review B 101 (2020) 020301(R).
[35] S.H. Mousavi, A.B. Khanikaev, Z. Wang, Topologically protected elastic waves in phononic metamaterials, Nat. Commun. 6 (2015) 8682.
[36] M.I.N. Rosa, R.K. Pal, J.R.F. Arruda, M. Ruzzene, Edge States and Topological Pumping in Spatially Modulated Elastic Lattices, Phys. Rev. Lett. 123 (3) (2019) 034301.
[37] M. Serra-Garcia, V. Peri, R. Süsstrunk, O.R. Bilal, T. Larsen, L.G. Villanueva, S.D. Huber, Observation of a phononic quadrupole topological insulator, Nature 555 (7696) (2018) 342–345.
[38] H. Xue, Y. Yang, F. Gao, Y. Chong, B. Zhang, Acoustic higher-order topological insulator on a kagome lattice, Nat. Mater. 18 (2) (2019) 108–112.
[39] X.-W. Luo, C. Zhang, Higher-Order Topological Corner States Induced by Gain and Loss, Phys. Rev. Lett. 123 (7) (2019) 073601.
[40] Y. Ota, F. Liu, R. Katsumi, K. Watanabe, K. Wakabayashi, Y. Arakawa, S. Iwamoto, Photonic crystal nanocavity based on a topological corner state, Optica 6 (6) (2019) 786, https://doi.org/10.1364/OPTICA.6.000786.
[41] R. Jackiw, P. Rossi, Zero modes of the vortex-fermion system, Nucl. Phys. B 190 (4) (1981) 681–691.
[42] P. Gao, D. Torrent, F. Cervera, P. San-Jose, J. Sanchez-Dehesa, J. Christensen, Majorana-like zero modes in Kekulé distorted sonic lattices, Phys. Rev. Lett. 123 (2019), 196601.

[43] C.-W. Chen, N. Lera, R. Chaunsali, D. Torrent, J.V. Alvarez, J. Yang, P. San-Jose, J. Christensen, Mechanical analogue of a Majorana bound state, Adv. Mater. 31 (51) (2019) 1904386.
[44] X. Gao, L. Yang, H. Lin, L. Zhang, J. Li, F. Bo, Z. Wang, L. Lu, Dirac-vortex topological cavities, Nat Nanotechnol 15 (2020) 1012–1018.
[45] Z. Zhang, Q. Wei, Y. Cheng, T. Zhang, D. Wu, X. Liu, Topological creation of acoustic pseudospin multipoles in a flow-free symmetry-broken metamaterial lattice, Phys. Rev. Lett. 118 (2017), 084303.
[46] C.Y. Hou, C. Chamon, C. Mudry, Electron fractionalization in two-dimensional graphenelike structures, Phys. Rev. Lett. 98 (2007), 186809.
[47] P. Gao, J. Christensen, Topological sound pumping of zero-dimensional bound states, Advanced Quantum Technologies 3 (2020) 2000065.
[48] A.J. Menssen, J. Guan, D. Felce, M.J. Booth, I.A. Walmsley, Photonic topological mode bound to a vortex, Phys. Rev. Lett. 125 (2020), 117401.
[49] G.J. Chaplain, J.M. De Ponti, G. Aguzzi, A. Colombi, R.V. Craster, Topological rainbow trapping for elastic energy harvesting in graded Su-Schrieffer-Heeger systems, Phys. Rev. Appl 14 (2020), 054035.
[50] Z. Zhang, Y. Cheng, X. Liu, Achieving acoustic topological valley-Hall states by modulating the subwavelength honeycomb lattice, Sci. Rep. 8 (2018) 16784.
[51] R. Chaunsali, C.-W. Chen, J. Yang, Subwavelength and directional control of flexural waves in zone-folding induced topological plates, Physical Review B 97 (2018), 054307.
[52] V.A. Li-Yang Zheng, Z.-G. Chen, O. Richoux, G. Theocharis, J.M. YingWu, Simon Felix, Vincent Tournat, Vincent Pagneux, Acoustic graphene network loaded with Helmholtz resonators a first-principle modeling, Dirac cones, edge and interface waves, New J. Phys. 22 (2020), 013029.
[53] E.J.P. Miranda Jr, E.D. Nobrega, S.F. Rodrigues, C. Aranas Jr, J.M.C. Dos Santos, Wave attenuation in elastic metamaterial thick plates: analytical, numerical and experimental investigations, Int. J. Solids Struct. 204–205 (2020) 138–152.
[54] I.E. Elishakoff, Handbook on Timoshenko-Ehrenfest Beam and Uflyand-Mindlin Plate Theories, World Scientific, 2019.
[55] Y. Xiao, J. Wen, X. Wen, Broadband locally resonant beams containing multiple periodic arrays of attached resonators, Phys. Lett. A 376 (2012) 1384–1390.
[56] Y. Xiao, J. Wen, X. Wen, Flexural wave band gaps in locally resonant thin plates with periodically attached spring–mass resonators, J. Phys. D Appl. Phys. 45 (2012), 195401.
[57] E.J.P. Miranda, E.D. Nobrega, A.H.R. Ferreira, J.M.C. Dos Santos, Flexural wave band gaps in a multi-resonator elastic metamaterial plate using Kirchhoff-Love theory, Mech. Syst. Sig. Process. 116 (2019) 480–504.
[58] E.J.P.M. Jr, J.M.C. Dos Santos, Flexural wave band gaps in multi-resonator elastic metamaterial Timoshenko beams, Wave Motion 91 (2019), 102391.
[59] L.H. Wu, X. Hu, Scheme for achieving a topological photonic crystal by using dielectric material, Phys. Rev. Lett. 114 (2015), 223901.
[60] D. Torrent, D. Mayou, J. Sánchez-Dehesa, Elastic analog of graphene: Dirac cones and edge states for flexural waves in thin plates, Physical Review B 87 (2013), 115143.
[61] D.T. Natalia Lera, P. San-Jose, J. Christensen, J.V. Alvarez, Valley Hall phases in kagome lattices, Physical Review B 99 (2019), 134102.
[62] L. He, Z. Wen, Y. Jin, D. Torrent, X. Zhuang, T. Rabczuk, Inverse design of topological metaplates for flexural waves with machine learning, Mater. Des. 199 (2020), 109390.
[63] P. Gao, A. Climente, J. Sánchez-Dehesa, L. Wu, Single-phase metamaterial plates for broadband vibration suppression at low frequencies, J. Sound Vib. 444 (2019) 108–126.
[64] P. Gao, A. Climente, J. Sánchez-Dehesa, L. Wu, Theoretical study of platonic crystals with periodically structured N-beam resonators, J. Appl. Phys. 123 (2018), 091707.
[65] Z. Wen, S. Zeng, D. Wang, Y. Jin, B. Djafari-Rouhani, Robust edge states of subwavelength chiral phononic plates, Extreme Mech. Lett. 44 (2021), 101209.